2008 IEEE International Conference on
Robotics and Automation
Pasadena, CA, USA, May 19-23, 2008

Modeling Assembled-MEMS Microrobots for Wireless Magnetic Control

Zoltán Nagy, Olgaç Ergeneman, Jake J. Abbott, Marco Hutter, Ann M. Hirt, and Bradley J. Nelson

Abstract— **Capitalizing on advances in CMOS and MEMS technologies, microrobots have the potential to dramatically change many aspects of medicine by navigating bodily fluids to perform targeted diagnosis and therapy. Onboard energy storage and actuation is very difficult at the microscale, but externally applied magnetic fields provide an unparalleled means of wireless power and control. Recent results have provided a model for accurate real-time control of soft-magnetic bodies with axially symmetric geometries. In this paper, we extend the model to consider the real-time control of assembled-MEMS devices that may have significantly more complex geometries. We validate the model through FEM and experiments. The model captures the characteristics of complex 3-D structures and allows us, for the first time, to consider full 6-DOF control of untethered devices, which can act as *in vivo* microrobots or as end-effectors of micromanipulation systems.**

I. INTRODUCTION

There is a strong interest in minimally invasive medical diagnosis and therapy, and improvements in CMOS and MEMS technologies will enable further miniaturization of medical devices [1], [2]. Wireless microrobots that are capable of navigating bodily fluids to perform localized sensing or targeted drug delivery will open the door to a variety of new diagnostic and therapeutic procedures. These untethered devices can be used in parts of the body that are currently inaccessible or too invasive to access. Energy storage and onboard actuation mechanisms at the scale of these microrobots are currently insufficient to generate the forces and torques required to move through bodily fluids. The most promising method of providing wireless power and control for *in vivo* microrobots is through magnetic fields generated by external sources [3]–[7].

There is a significant body of work dealing with non-contact magnetic manipulation of permanent magnets, where the magnetization of the device is effectively independent of the applied field. However, the fabrication of permanent magnets at the microscale involves nonstandard MEMS processes, and the initial magnetization is difficult. Compared to permanent magnets, soft-magnetic materials provide easier fabrication, as well as increased flexibility in control. They have been previously used in the fabrication of end-effectors of untethered micromanipulation systems [8]. In addition, they provide increased safety in biomedical applications as they are magnetically inert in the absence of magnetic fields. However, with soft-magnetic materials, the magnetization of the body is a nonlinear function of the applied magnetic field, and the relationship between the applied field and the resulting torque and force is non-trivial. A model for real-time control of soft-magnetic bodies with axial symmetry was recently presented by Abbott et al. [9]. However, with such a shape, generation of magnetic torque about its axis of symmetry is not possible. Microrobots with more complex shapes that do not exhibit axial symmetry, and consequently have the potential for full 6-DOF control, require an extension of the model.

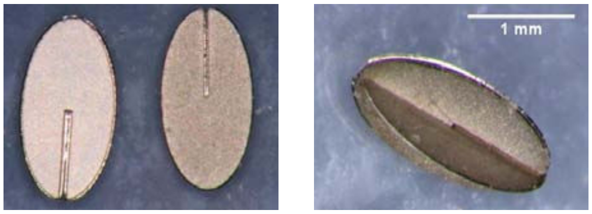

(a) Individual nickel parts (b) Assembled microrobot

Fig. 1. Relatively simple 2-D parts can be assembled into complex 3-D structures. The parts shown have dimensions 2.0 mm × 1.0 mm × 42 µm, and can be further miniaturized.

Fabricating truly 3-D mechanical structures at the microscale is challenging. With current MEMS fabrication methods, mechanical parts are built using 2-D (planar) geometries with desired thickness. Three-dimensional structures can be obtained by bending or assembling these planar parts (Fig. 1), and it has been demonstrated that very complex structures can be built with such methods [10]–[12]. Assembled-MEMS microrobots have the potential to provide increased functionality over simpler geometries. Yesin et al. [4] recently developed a microrobot that is assembled from electroplated nickel components, and 2-DOF magnetic control (1-DOF rotation, 1-DOF translation) was demonstrated in a planar fluid-filled maze. Researchers have developed models of soft-magnetic MEMS microactuators with simple geometries [13]. However, there is no prior work on modeling the magnetic properties of assembled structures, which is needed for precise control of untethered devices. Finite element methods (FEM) can be used to model magnetic behavior of arbitrary assemblies, but are impractical in real-time control of magnetic devices because of long computation times.

This work is aimed at those interested in modeling magnetic force and torque on soft-magnetic MEMS devices, including assembled structures, for real-time control. The contributions of this work are as follows. First, the problem of determining the magnetization of a soft-magnetic body is formulated as a global minimization problem. Capitalizing

---

This work is supported by the NCCR Co-Me of the Swiss National Science Foundation.

The authors are with the Institute of Robotics and Intelligent Systems, ETH Zurich, Switzerland, except A. M. Hirt is with the Institute of Geophysics, ETH Zurich. Z. Nagy is the corresponding author (`nagyz@ethz.ch`).

978-1-4244-1647-9/08/$25.00 ©2008 IEEE.

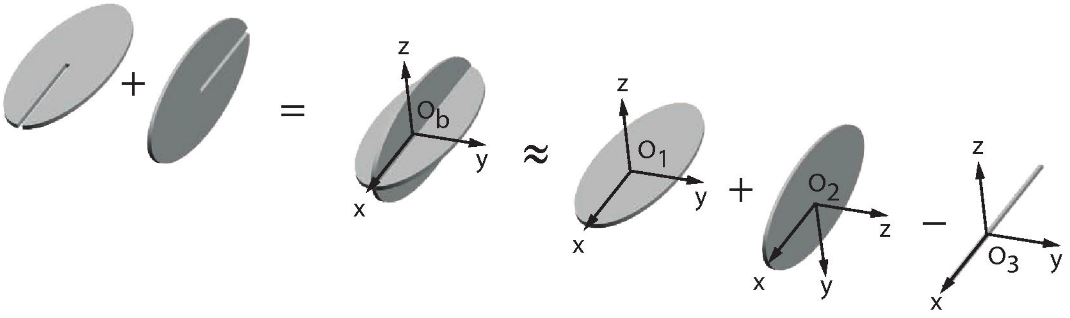

Fig. 2. Microfabricated nickel parts (left) are assembled to form a microrobot (middle). The body frame is assigned to the microrobot arbitrarily. For the computation, rather than using the actual complex shapes of the parts, we consider the microrobot as a superposition of simpler geometries (right). The frames of the individual parts are assigned with the x-axis along the longest dimension of the body and with the z-axis along the shortest dimension.

on the structure of the problem, we reformulate the global minimization problem as a simple polynomial root solving problem. This allows us to decrease the computation time, which is important for real-time applications. We demonstrate that assembled devices can be modeled as the superposition of simple geometries. We use a description that is free of parameterizations, enabling singularity-free computation for 6-DOF control of untethered devices. Finally, we validate the proposed method experimentally and numerically with a microrobot assembled from electroplated nickel parts.

II. MODELING ASSEMBLED-MEMS MICROROBOTS

In this work we consider microrobots that consist of n thin soft-magnetic parts that are microfabricated in a planar process, and then microassembled to form a 3-D structure as shown in Figs. 1 and 2. If the microrobot is placed in an arbitrary magnetic field $\mathbf{H} = [h_x, h_y, h_z]^T$ (expressed in the frame of the assembled body, with units A/m), its parts are magnetized. In general, the magnetization of the parts will mutually interact, and the determination of the resulting magnetization is a complex problem. Knowledge of magnetization is required to calculate magnetic forces and torques exerted on the microrobot. To compute the magnetization, we will make two basic assumptions. First, we will neglect the magnetic interaction between the individual pieces, and second, to ease the computation, rather than using the actual complex shapes of the parts, we consider the microrobot as a superposition of simpler geometries as shown in Fig. 2. We compute the total force ${}^b\mathbf{F}_b$ and torque ${}^b\mathbf{T}_b$ on the microrobot as the sum of the individual forces and torques:

$$ {}^b\mathbf{F}_b = \sum_{k=1}^{n} {}^b\mathbf{F}_k = \sum_{k=1}^{n} {}^bR_k {}^k\mathbf{F}_k \tag{1} $$

$$ {}^b\mathbf{T}_b = \sum_{k=1}^{n} {}^b\mathbf{T}_k = \sum_{k=1}^{n} {}^bR_k {}^k\mathbf{T}_k \tag{2} $$

where ${}^bR_k$ is the rotation matrix describing the orientation of the k^{th} part with respect to the body frame, and ${}^k\mathbf{F}_k$ and ${}^k\mathbf{T}_k$ are the force and torque acting on the k^{th} part calculated in its own frame. The computation of the latter is the topic of the next section. Then, in Section IV we validate our model both experimentally and numerically.

III. MODELING AN INDIVIDUAL PART

Vectors in this section are described with respect to the frame of the single part. Basic magnetic results applied in this section can be found in standard texts [14]–[16]. The applied field $\mathbf{H}$ is the source of the magnetization $\mathbf{M}$ of the soft-magnetic material. Once $\mathbf{M}$ is known, the force and torque acting on the body can be computed as

$$ \mathbf{F} = \mu_0 \int_v (\mathbf{M}\cdot\nabla)\mathbf{H}\,\mathrm{d}\nu \approx \mu_0 v(\mathbf{M}\cdot\nabla)\mathbf{H} \tag{3} $$

$$ \mathbf{T} = \mu_0 \int_v (\mathbf{M}\times\mathbf{H})\,\mathrm{d}\nu \approx \mu_0 v\mathbf{M}\times\mathbf{H} \tag{4} $$

where v is the volume of the piece and $\mu_0 = 4\pi \times 10^{-7}$ Tm/A is the permeability of free space. Note that the applied field can also be expressed in units T using $\mathbf{B} = \mu_0\mathbf{H}$. In the integral expressions, $\mathbf{M}$ and $\mathbf{H}$ generally vary over the body. The simplifying expressions consider only $\mathbf{H}$ at the center of mass of the body, which is an adequate assumption when the body is small compared to spatial changes in the applied field, and treat $\mathbf{M}$ as a constant vector, which is only true for ellipsoids but facilitates real-time computation. Equation (3) is a compact notation for a complex operation. However, since there is no electric current flowing through the region occupied by the body, Maxwell's equation provide the constraint $\nabla \times \mathbf{H} = 0$. This allows us to express (3) in a more intuitive form:

$$ \mathbf{F} = \mu_0 v \left[\mathbf{M}\cdot\frac{\partial\mathbf{H}}{\partial x}, \quad \mathbf{M}\cdot\frac{\partial\mathbf{H}}{\partial y}, \quad \mathbf{M}\cdot\frac{\partial\mathbf{H}}{\partial z} \right]^T \tag{5} $$

The magnitude of $\mathbf{M}$ is a nonlinear function of the applied field. It has been shown that ideal soft-magnetic materials (i.e., ferromagnetic materials with negligible hysteresis) can be modeled by

$$ |\mathbf{M}| = m_s \mathcal{L}\left(\alpha|\mathbf{H_i}|\right) \tag{6} $$

where $\mathcal{L}(x)$ is the Langevin function given by

$$ \mathcal{L}(x) = \coth x - \frac{1}{x}, \tag{7} $$

α is an empirical parameter in m/A related to the susceptibility (or permeability), m_s is the saturation magnetization (in A/m), and $\mathbf{H_i}$ is the internal field. It satisfies

$$ \mathbf{H_i} = \mathbf{H} - \mathbf{H_d} = \mathbf{H} - N\mathbf{M} \tag{8} $$

where $\mathbf{H_d}$ is the demagnetizing field, related to the magnetization through the positive-definite demagnetizing tensor N.

We define the frame along the principle axes of the body, such that N is diagonal (i.e., $N = \mathrm{diag}(n_1, n_2, n_3)$). The elements of N are the demagnetizing factors of the piece, with $\mathrm{tr}(N) = 1$. For uniqueness, we require that $n_1 \leq n_2 \leq n_3$. This means that the x-axis (corresponding to n_1) is the longest axis of the part, which is the easy axis of magnetization; the z-axis (corresponding to n_3) is the shortest axis of the part, which is the hard axis of magnetization (see Fig. 2). In this work we use formulas provided in [17] to find the equivalent ellipsoid of shapes that can be characterized by up to two non-dimensional parameters (e.g. prisms, cylinders, elliptical cylinders), since demagnetizing factors can only be calculated analytically for ellipsoids. This allows us to consider a variety of geometries for the individual microfabricated parts.

The direction and magnitude of $\mathbf{M}$ minimize the magnetic energy density (in J/m^3)

$$e = \frac{1}{2}\mu_0 \mathbf{M}^T N \mathbf{M} - \mu_0 \mathbf{H}^T \mathbf{M}. \tag{9}$$

The first term in (9) is the demagnetizing energy due to shape anisotropy, which tends to align $\mathbf{M}$ with the easy axis of the piece. The second term is minimized when $\mathbf{M}$ is aligned with $\mathbf{H}$. Other energies, such as crystalline anisotropy and exchange energy, are neglected in our case [14].

Since N is positive definite, e is convex and has a global minimum [18]. Thus, the determination of the magnetization is described by the minimization problem

$$\begin{array}{ll} \text{minimize} & \frac{1}{2}\mathbf{M}^T N \mathbf{M} - \mathbf{H}^T \mathbf{M} \\ \text{subject to} & \mathbf{M}^T \mathbf{M} - m_{\text{max}}^2 \leq 0 \end{array}$$

where

$$m_{\text{max}} = m_s \mathcal{L}\left(\alpha |\mathbf{H}|\right) \tag{10}$$

is an upper limit for the magnitude of $\mathbf{M}$ for a given field strength $|\mathbf{H}|$. It can be shown that $|\mathbf{H_i}| \leq |\mathbf{H}|$. Since the Langevin function (6) is monotonically increasing, we have

$$m_s \mathcal{L}\left(\alpha |\mathbf{H_i}|\right) \leq m_s \mathcal{L}\left(\alpha |\mathbf{H}|\right) < m_s. \tag{11}$$

Thus, for a given applied field $\mathbf{H}$, we can compute a conservative upper limit for the magnitude of $\mathbf{M}$, without the knowledge of $\mathbf{H_i}$.

Convex minimization problems [18], [19] can be carried out using a nonlinear minimization tool such as MATLAB's function `fmincon`. In a real-time control system, the minimization has to be computed within a single control loop. Although a global minimization algorithm will converge, we can speed up the computation by analyzing the problem more closely. We introduce a Lagrange multiplier:

$$L(\mathbf{M}, \lambda) = \frac{1}{2}\mathbf{M}^T N \mathbf{M} - \mathbf{H}^T \mathbf{M} + \lambda(\mathbf{M}^T \mathbf{M} - m_{\text{max}}^2). \tag{12}$$

Since we consider a convex problem, the necessary and sufficient conditions for the minimum are

$$\frac{\partial L}{\partial \mathbf{M}} = N\mathbf{M} - \mathbf{H} + 2\lambda \mathbf{M} = \mathbf{0} \tag{13}$$

and

$$\frac{\partial L}{\partial \lambda} = \mathbf{M}^T \mathbf{M} - m_{\text{max}}^2 \leq 0 \tag{14}$$

with

$$\lambda \begin{cases} \geq 0, & \mathbf{M}^T \mathbf{M} - m_{\text{max}}^2 = 0, \\ = 0, & \mathbf{M}^T \mathbf{M} - m_{\text{max}}^2 < 0. \end{cases} \tag{15}$$

Evaluating (13), we find the solution to the minimization problem to be

$$\mathbf{M} = \left(N + 2\lambda I\right)^{-1} \mathbf{H}. \tag{16}$$

Evaluating (14) for $\lambda > 0$ yields

$$\mathbf{H}^T \left(N + 2\lambda I\right)^{-2} \mathbf{H} - m_{\text{max}}^2 = 0. \tag{17}$$

It can be shown that $\lambda = \max\{0, \bar{\lambda}\}$ where $\bar{\lambda}$ is the largest real solution of (17). Expanding (17) yields

$$\frac{h_x^2}{(n_1 + 2\lambda)^2} + \frac{h_y^2}{(n_2 + 2\lambda)^2} + \frac{h_z^2}{(n_3 + 2\lambda)^2} - m_{\text{max}}^2 = 0. \tag{18}$$

Rationalizing (18), we find that solving it is equivalent to solving for the roots of a sixth-order polynomial in λ:

$$c_6 \lambda^6 + c_5 \lambda^5 + \cdots + c_1 \lambda + c_0 = 0, \tag{19}$$

where the coeffcents c_j are algebraic functions of h_x, h_y, h_z, n_1, n_2, n_3, and m_{max} that can be derived analytically and stored in a function. We can use a root solver, such as the `roots` function of MATLAB, that uses the c_j's as inputs, to compute $\bar{\lambda}$, which is now the largest real root of (19). This algorithm considers the structure of the problem, in that it treats the polynomial as a characteristic polynomial of some matrix, and its roots as the eigenvalues of this matrix. Therefore, the computation of $\bar{\lambda}$ (and consequently of $\mathbf{M}$) by finding the eigenvalues of this matrix is faster than a global minimization algorithm. In fact, we find in our calculations that it is at least an order of magnitude faster. Thus, we have converted the global minimization problem into a simple polynomial root-solving problem.

Assuming $\lambda > 0$, it can be shown that:

$$0 < \lambda \leq \frac{1}{2}\left(\frac{|\mathbf{H}|}{m_{\text{max}}} - n_1\right) \tag{20}$$

where n_1 is the smallest demagnetizing factor in our convention. Solving the outer inequality for $|\mathbf{H}|$ we find

$$|\mathbf{H}| \geq m_{\text{max}} n_1. \tag{21}$$

In the envisaged application this limit can be precomputed. If any field is applied below this limit, no root solving is necessary, and we can use (16) with $\lambda = 0$.

Note that under the assumption of linear material behavior, the standard result for the magnetization is $\mathbf{M} = \mathcal{X}_a \mathbf{H}$, where $\mathcal{X}_a$ is the apparent (or external) susceptibility matrix

$$\mathcal{X}_a = \left(I + \chi N\right)^{-1} \chi \tag{22}$$

with χ as the susceptibility of the material [16]. Note however, that $\mathcal{X}_a$ reduces to N^{-1} for $\chi n_i \gg 1\, \forall i$, which is a reasonable assumption for the case of soft-magnetic materials and the shapes that we consider in this work. This situation is accurately captured by our model, as material behavior for low applied fields corresponds to $\lambda = 0$ and our solution then is $\mathbf{M} = N^{-1}\mathbf{H}$.

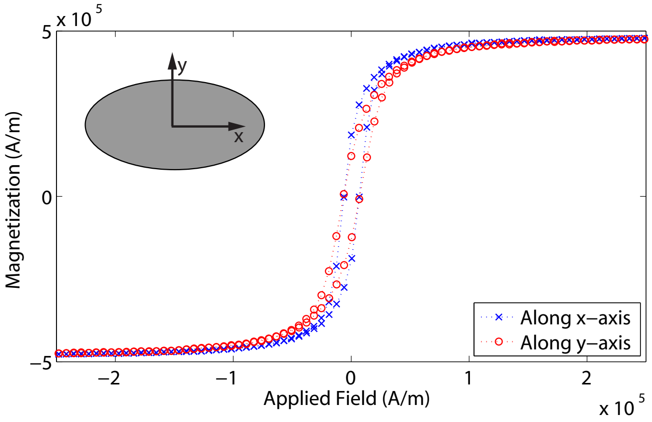

(a) Original data taken along two axes

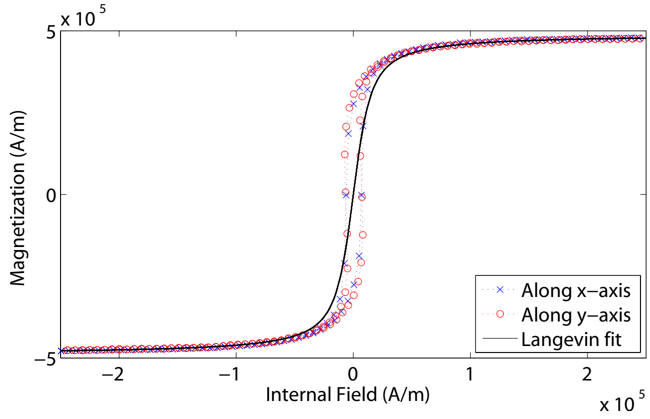

(b) Data corrected for shape effects using known demagnetizing factors, and the best Langevin Fit.

Fig. 3. Magnetization data taken with a vibrating-sample magnetometer is used to determine the intrinsic material properties.

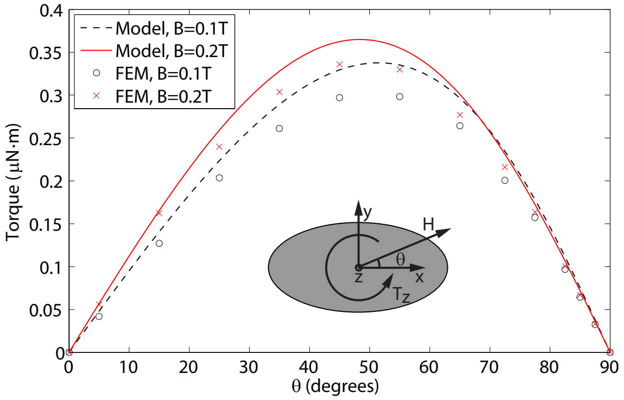

(a) Torque about z-axis versus applied field angle. The field is applied in the xy-plane.

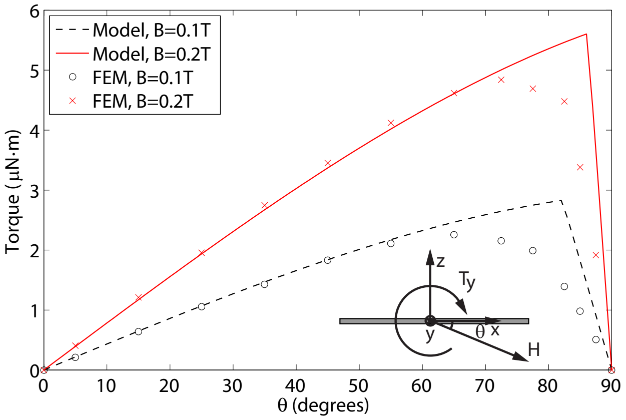

(b) Torque about y-axis versus applied field angle. The field is applied in the xz-plane.

Fig. 4. Comparison of analytical model and FEM simulations for the torque on a single part. Insets show the orientation of the applied field and the resulting torque.

IV. EXPERIMENTAL AND FEM VALIDATION

A. *Magnetization*

Elliptical parts with a length of 2.0 mm, a width of 1.0 mm, and a thickness of 42 µm were formed by electroplating nickel. The details of the fabrication steps can be found in [4]. Magnetization data was then collected with a MicroMag 3900 vibrating-sample magnetometer (VSM) from Princeton Measurements Corp. Figure 3(a) shows the magnetization along the x and y axes plotted against the applied field.

We then corrected for the shape by computing the internal field according to (8). This requires knowledge of the demagnetizing tensor, which we find using the method described in [17] to be

$$N = \text{diag}\left(0.02439, 0.06405, 0.9115\right). \tag{23}$$

Figure 3(b) shows the magnetization plotted against the internal field. The shape effects have been corrected for, as both curves coincide, and we are left with the intrinsic material properties. Figure 3(b) also shows the Langevin fit with $\alpha = 1.71 \times 10^{-4}$ m/A and $m_s = 4.89 \times 10^5$ A/m. Note that, by using a Langevin function, hysteresis is neglected. These material properties are used in all subsequent analytical computations and in the FEM package Maxwell 3D.

B. *Individual Part*

As a preliminary validation step, we compare our analytical model to FEM results for a single part. For the elliptical part described in Section IV-A, we compute the torque around its z-axis when the field is applied in the xy-plane, as well as around its y-axis when the field is applied in the xz-plane. Figure 4 shows the results. We find good agreement between the FEM results and our model, with the analytical model slightly overpredicting the FEM results. We also observe that applying the field out of the plane of the part results in torques that are an order of magnitude larger than when the field is applied in the plane of the part. We have validated the model of Section III, and we will now validate the assembled-MEMS model of Section II.

C. *Assembled-MEMS Microrobot*

A microrobot was assembled from elliptical nickel parts as shown in Fig. 1. We assign a body frame and the individual component frames as shown in Fig. 2. By inspection we find the rotation matrices to be

$$ {}^{b}R_1 = {}^{b}R_3 = I, \qquad {}^{b}R_2 = \begin{bmatrix} 1 & 0 & 0 \\ 0 & 0 & 1 \\ 0 & -1 & 0 \end{bmatrix} \tag{24} $$

In our simplifying model, we consider two parts being elliptical with the sizes given in Section IV-A, resulting in the same demagnetizing tensor

$$ N_1 = N_2 = \mathrm{diag}\,(0.02439, 0.06405, 0.9115)\,. \tag{25} $$

The third part is a rectangular prism with a length of 2 mm, and a width and height of 42 μm. Again, we find the demagnetizing tensor using the method from [17] to be

$$ N_3 = \mathrm{diag}\,(0.009867, 0.4951, 0.4951)\,. \tag{26} $$

We measure magnetic torque using a custom-built torque magnetometer [20], which works by applying a uniform field at a desired angle with respect to the microrobot. We investigate two situations. In the first, the fields are applied in the xy-plane and the torque around the z-axis is measured. In the second, the fields are applied in the yz-plane and the torque around the x-axis is measured. The results are shown in Fig. 5, along with corresponding analytical and FEM results. We see very good agreement between the experimental data and the FEM results. Generally, we find good agreement between our analytical model (the only available model) and the experimental data, with the analytical model again overpredicting the measured torque. This overprediction of torque in certain configurations and at certain applied-field angles is due to the simplifying assumptions that were made to facilitate real-time computation. Alternatives that improve accuracy but incur little additional computational load are currently under investigation.

We observe that the magnitude of the torques in Fig. 4(b) and Fig. 5(a) are almost identical. In addition, recall that the torque in Fig. 4(b) is an order of magnitude larger than the torque in Fig. 4(a). Thus, the torque on the whole microrobot is essentially provided by the part to which the applied field is out of plane. We conclude that there are specific configurations where one part is dominating the behavior of the assembled structure, and the contribution of the other part is negligible.

In Fig. 5(b) we observe that for very low fields the torque is predicted to be zero by the FEM results and our model (the field B=0.01T is below the rest field of the torque magnetometer, so no experimental data is available). This is due to the torques on the individual parts essentially canceling each other out. So for these fields, the torque along the long axis of the microrobot vanishes like the torque around the long axis of a body with axial symmetry. However, increasing the applied field leads to different magnetizations and hence different torques on the individual parts. Therefore a net torque is exerted on the microrobot. This net torque vanishes at 0° and 45°, which is expected from the symmetry of the microrobot.

Next, force measurements were taken using a custom-built measurement system [21]. The magnetic force is measured as a function of the distance between the microrobot and a permanent magnet whose field is accurately characterized. The x-axis of the microrobot is aligned with the dipole axis of the magnet, and the microrobot is moved along the dipole axis as shown in Fig. 6. We observe that our model accurately predicts the magnetic force on the microrobot.

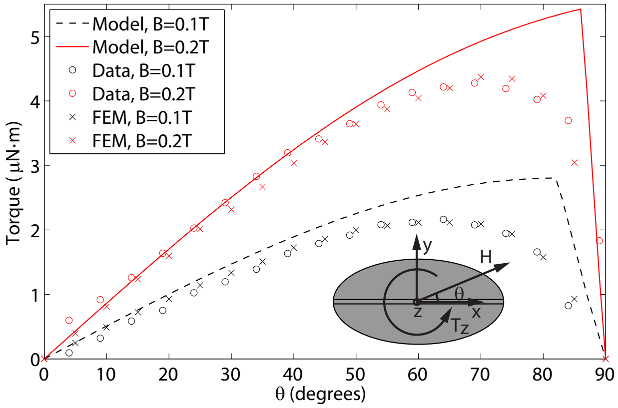

(a) Torque about z-axis versus applied field angle. The field is applied in the xy-plane.

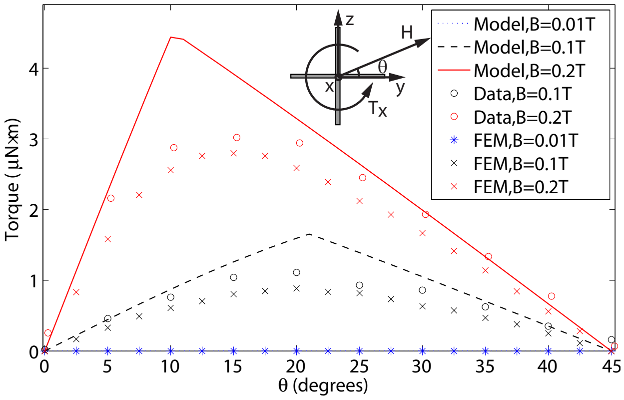

(b) Torque about x-axis versus applied field angle. The field is applied in the yz-plane. Note that the model and FEM predict zero torque for sufficiently low field magnitude.

Fig. 5. Comparison of analytical model, FEM simulations, and experimental data for the torque on an assembled microrobot. Insets show the orientation of the applied field and the resulting torque.

V. CONCLUSIONS

We presented a method for the fast computation of magnetic force and torque acting on a soft-magnetic 3-D assembled-MEMS device. For this, we first formulated the problem of determining the magnetization of the device as a global minimization problem and then reformulated it as a simple polynomial root solving problem. We validated the method by both FEM simulations and torque and force measurements on a microrobot assembled from electroplated nickel parts. The model captures the behavior of the individual parts, as well as the behavior of the assembled microrobot.

The proposed model captures the magnetic behavior of devices assembled from thin parts that are widely used in MEMS. In fact, most of the structures of interest fabricated

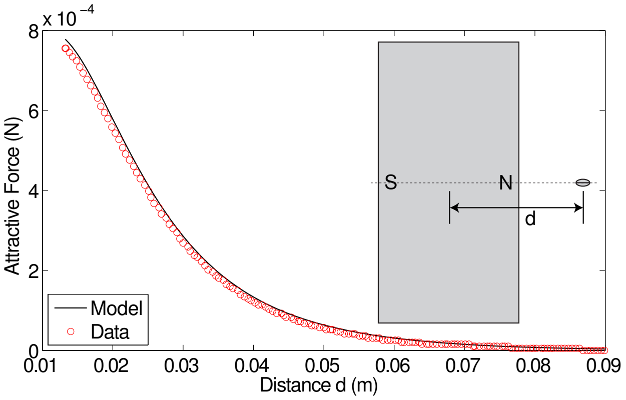

Fig. 6. Comparison of analytical model and experimental data for the force on an assembled microrobot. The left edge of the plot corresponds to the surface of the magnet. The inset illustrates the experimental setup, drawn with 1:1 scale to the data.

by MEMS processes will be similar to the planar parts analyzed in this work. Therefore, this method can be used to model a variety of MEMS devices, both tethered and untethered.

Our model provides the fundamental building block for a real-time control system for untethered devices. The microrobot actuation model can be used in feed-forward controllers, as well as in the design of feedback controllers. In addition, the model can be used in observers (i.e., Kalman filters) for localization. On a desktop PC (Pentium D, 2.80 GHz, 1GB RAM) the computation of the magnetization for a single part takes approximately 0.5 ms using the `roots` algorithm in MATLAB. This algorithm is computed for each of the simple components and the results are superimposed, giving a total force/torque computation of less than 2 ms. Thus, this model is fast enough to be used in real time within a larger control system.

Previous work does not allow for full 6-DOF control of magnetic devices due to the simplicity of the structures considered. For example, spherical bodies can be controlled with up to 3-DOF and axially symmetric bodies with up to 5-DOF [9]. Our model captures the characteristics of complex 3-D structures and allows us, for the first time, to consider full 6-DOF control of untethered devices. This will provide major advances in the control of *in vivo* biomedical devices, as well as in wireless micromanipulation systems.

Our current work focuses on the extension of the proposed model. Specifically, we are investigating how the model handles pieces with corners (i.e. nonelliptical), and for what assembled complex shapes the superposition is applicable.

VI. ACKNOWLEDGMENT

The authors would like to thank Michael Kummer for assistance with the force measurements, Wanfeng Yan for designing the microfabrication masks, and Salvador Pané i Vidal for fabrication and assembly of the nickel parts.

REFERENCES

[1] P. Dario, M. C. Carrozza, A. Benvenuto, and A. Menciassi, “Microsystems in biomedical applications,” *J. of Micromechanics and Microengineering*, vol. 10, pp. 235–244, 2000.

[2] Y. Haga and M. Esashi, “Biomedical microsystems for minimally invasive diagnosis and treatment,” *Proc. of the IEEE*, vol. 92, no. 1, pp. 98–114, 2004.

[3] K. Ishiyama, K. I. Arai, M. Sendoh, and A. Yamazaki, “Spiral-type micro-machine for medical applications,” *J. of Micromechatronics*, vol. 2, no. 1, pp. 77–86, 2003.

[4] K. B. Yesin, K. Vollmers, and B. J. Nelson, “Modeling and control of untethered biomicrorobots in a fluidic environment using electromagnetic fields,” *Int. J. Robot. Res.*, vol. 25, no. 5-6, pp. 527–536, 2006.

[5] S. Martel, J.-B. Mathieu, O. Felfoul, A. Chanu, E. Aboussouan, S. Tamaz, and P. Pouponneau, “Automatic navigation of an untethered device in the artery of a living animal using a conventional clinical magnetic resonance imaging system,” *Applied Physics Letters*, vol. 90, no. 11, pp. 114 105(1–3), 2007.

[6] O. Ergeneman, G. Dogangil, M. P. Kummer, J. J. Abbott, N. M. K., and N. B. J., “A magnetically controlled wireless optical oxygen sensor for intraocular measurements,” *IEEE Sensors Journal*, vol. 8, no. 1, pp. 29–37, 2008.

[7] J. J. Abbott, Z. Nagy, F. Beyeler, and B. J. Nelson, “Robotics in the small, part I: Microrobotics,” *IEEE Robot. Automat. Mag.*, vol. 14, no. 2, 2007.

[8] M. Gauthier and E. Piat, “An electromagnetic micromanipulation systems for single-cell manipulation,” *J. of Micromechatronics*, vol. 2, no. 2, pp. 87–119, 2004.

[9] J. J. Abbott, O. Ergeneman, M. P. Kummer, A. M. Hirt, and B. J. Nelson, “Modeling magnetic torque and force for controlled manipulation of soft-magnetic bodies,” *IEEE Trans. on Robotics*, vol. 23, no. 6, pp. 1247–1252, 2007.

[10] G. Yang, J. A. Gaines, and B. J. Nelson, “Optomechatronic design of microassembly systems for manufacturing hybrid microsystems,” *IEEE Trans. Ind. Electron.*, vol. 52, no. 4, pp. 1013–1023, 2005.

[11] E. Iwase and I. Shimoyama, “Multistep sequential batch assembly of three-dimensional ferromagnetic microstructures with elastic hinges,” *J. Microelectromech. Syst.*, vol. 14, no. 6, pp. 1265–1271, 2005.

[12] R. R. A. Syms, E. M. Yeatman, V. M. Bright, and G. M. Whitesides, “Surface tension-powered self-assembly of microstructures—the state-of-the-art,” *J. Microelectromech. Syst.*, vol. 12, no. 4, pp. 387–417, 2003.

[13] J. W. Judy and R. S. Muller, “Magnetically actuated, addressable microstructures,” *J. Microelectromech. Syst.*, vol. 6, no. 3, pp. 249–256, 1997.

[14] B. D. Cullity, *Introduction to Magnetic Materials*. Reading, MA: Addison-Wesley, 1972.

[15] A. Aharoni, *Introduction to the Theory of Ferromagnetism*, 2nd ed. New York: Oxford, University Press, 2000.

[16] R. C. O’Handley, *Modern Magnetic Materials: Principles and Applications*. New York: Wiley & Sons Inc., 2000.

[17] M. Beleggia, M. De Graef, and Y. T. Millev, “The equivalent ellipsoid of a magnetized body,” *J. Physics D*, vol. 39, no. 5, pp. 891–899, 2006.

[18] S. Boyd and L. Vandenberghe, *Convex Optimization*. Cambridge University Press, 2004.

[19] A. E. Bryson and Y. C. Ho, *Applied Optimal Control: Optimization, Estimation, and Control*. New York: Wiley, 1975.

[20] F. Bergmüller, C. Bärlocher, B. Geyer, M. Grieder, F. Heller, and P. Zweifel, “A torque magnetometer for measurements of the high-field anisotropy of rocks and crystals,” *Measurement Science and Technology*, vol. 5, no. 12, pp. 1466–1470, 1994.

[21] M. P. Kummer, J. J. Abbott, K. Vollmers, and B. J. Nelson, “Measuring the magnetic and hydrodynamic properties of assembled-MEMS microrobots,” in *Proc. IEEE Int. Conf. Robot. Automat.*, 2007, pp. 1122–1127.